Numerical Investigation of Flow and Starting Characteristics of Nozzle-Diffuser System for Plasma Wind Tunnel

Daesan Choi[1] and Kyu-Hong Kim[2]

Abstract. A plasma wind tunnel is a type of wind tunnel that can be used to simulate hypersonic and high-enthalpy flow environments on the ground. To start a wind tunnel, the wind tunnel must initially push the initial shock wave system from the nozzle throat into the diffuser throat. Compared with general supersonic wind tunnels, plasma wind tunnels require a higher pressure ratio to start, and problems such as wind tunnel unstarting may occur. Therefore, it is important to analyze issues associated with starting and to predict whether starting has commenced. In this study, the internal flow and starting characteristics of a nozzle-diffuser system for a plasma wind tunnel are investigated using a computational method. Flow analysis is performed before and after the wind tunnel is started by varying the back-pressure. Different from previous studies, the variation of total pressure is additionally confirmed, and hysteresis appeared before and after starting was analyzed. The flow conditions at the reservoir are a total pressure of 28.6 bar and a total temperature of 2,216 K, which generated a mass flow rate of approximately 2 kg/s with a Mach 7 nozzle, consistent with the conditions of a several-megawatt-class large plasma wind tunnel.

Keywords: Plasma wind tunnel; Wind tunnel starting; Hypersonic flow; Diffuser; Hysteresis

Nomenclature

x, y	=	axial displacement, radial displacement
Q	=	conservative variable vector
E, F	=	convective flux vector in axial direction, convective flux vector in radial direction
E_v, F_v	=	diffusive flux vector in axial direction, diffusive flux vector in radial direction
H	=	additional convective source vector describing axisymmetric flow
H_v	=	additional diffusive source vector describing axisymmetric flow
ρ	=	density
u, v	=	axial velocity and radial velocity
e_t	=	total energy
p	=	pressure
h	=	enthalpy
τ	=	stress tensor
μ, λ	=	viscosity coefficient, second viscosity coefficient
μ_l, μ_t	=	molecular viscosity coefficient, eddy viscosity coefficient
$\dot{q}$	=	heat transfer rate
Pr	=	Prandtl number

[1] Daesan Choi (✉)
R&D Center, NEXTfoam CO., LTD., Seoul, South Korea
e-mail: wooang7031@naver.com

[2] Kyu-Hong Kim (✉)
Department of Mechanical and Aerospace Engineering, Seoul National University, Seoul, South Korea
Institute of Advanced Aerospace Technology, Seoul National University, Seoul, South Korea
e-mail: aerocfd1@snu.ac.kr

κ = thermal conductivity
γ = specific heat ratio of calorically perfect air
$\tilde{\gamma}$ = specific heat ratio of thermal and chemical equilibrium air
k = turbulent kinetic energy
ε = turbulent dissipation rate
$\vec{V}$ = velocity vector
$\bar{\bar{E}}$ = strain rate tensor
P_0 = total pressure
T_0 = total temperature
$\dot{m}$ = mass flow rate
M = Mach number

1 Introduction

A plasma wind tunnel, as illustrated in Fig. 1, is a type of wind tunnel that can be used to simulate hypersonic and high-enthalpy flow environments on the ground. In a plasma wind tunnel, high-temperature gas is generated through a plasma generator, the heated gas is accelerated to a high speed through a nozzle, and the flow is ejected into the test section. The ejected gas is compressed through a diffuser and then passed through a heat exchanger and vacuum facility.

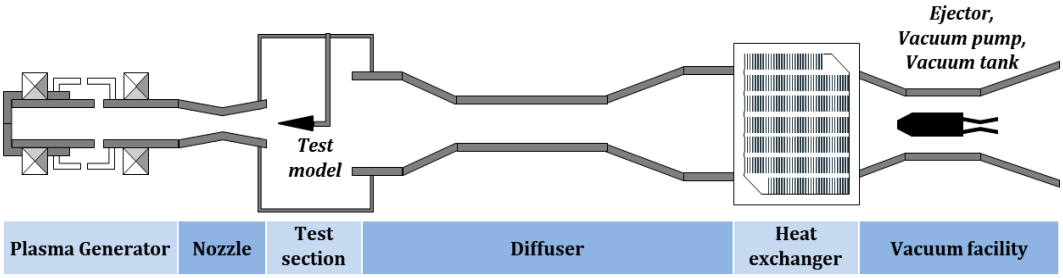

Fig. 1. Schematic illustration of plasma wind tunnel

Compared with conventional supersonic wind tunnels, plasma wind tunnels require a high pressure ratio between the reservoir and the diffuser exit to start and operate [1]; additionally, they are typically intended for continuous long-term operations [2]. Therefore, in general, a relatively high cost is required for the construction and operation of a plasma wind tunnel. Furthermore, whether the plasma wind tunnel can start, as well as the prediction of the pressure ratio that allows an efficient operation are important considerations for reducing construction and operating costs as well as for ensuring stable testing.

For a wind tunnel to start, the wind tunnel must initially push the initial shock wave system from the nozzle throat into the diffuser throat. At this time, a sufficient pressure ratio is required; in particular, a plasma wind tunnel requires a much higher pressure ratio compared with a typical supersonic wind tunnel. This is because the internal flow of a plasma wind tunnel exhibits a high Mach number and a low Reynolds number, where excess total pressure loss occurs owing to strong shock and shock-boundary layer interactions [1, 3]. Moreover, these characteristics render it difficult to analyze the internal flow and predict the starting conditions.

Hence, studies associated with plasma wind tunnels focusing on the pressure ratio and pressure recovery for wind tunnel operation have been conducted [1, 2, 4], and studies addressing the wind tunnel unstarting problem have been reported recently [5]. However, compared with the general supersonic wind tunnel, studies associated with plasma wind tunnels have not been sufficiently conducted, and relevant information is often limited.

In this study, the internal flow and starting characteristics of a nozzle-diffuser system for a plasma wind tunnel were investigated using a computational method. The flow conditions at the reservoir were a total pressure of 28.6 bar and a temperature of 2,216 K, which generated a mass flow rate of approximately 2 kg/s with a Mach 7 nozzle, consistent with the conditions of a several-megawatt-class large plasma wind tunnel. The Reynolds-averaged Navier–Stokes (RANS) equations were solved using a two-equation turbulence model and the modeling of equilibrium-state air considering the flow condition.

We analyzed flow characteristics such as the degree of expansion at the nozzle exit, test section conditions, and shock wave structure in a plasma wind tunnel. In particular, flow analysis was performed before and after the start of the wind tunnel by varying the back-pressure. Different from previous studies, the variation of total pressure is additionally confirmed, and hysteresis appeared before and after starting was analyzed. This study is expected to contribute to the limited literature pertaining to plasma wind tunnels.

2 Materials and Methods

2.1 Governing Equations

The governing equations used in this study were the axisymmetric compressible Reynolds Averaged Navier-Stokes (RANS) equations, as follows:

$$\frac{\partial Q}{\partial t}+\frac{\partial E}{\partial x}+\frac{\partial F}{\partial y}+H=\frac{\partial E_v}{\partial x}+\frac{\partial F_v}{\partial y}+H_v, \tag{1}$$

$$Q=\begin{bmatrix}\rho\\ \rho u\\ \rho v\\ \rho e_t\end{bmatrix}, \tag{2}$$

$$E=\begin{bmatrix}\rho u\\ \rho u^2+p\\ \rho uv\\ (\rho e_t+p)u\end{bmatrix}, F=\begin{bmatrix}\rho v\\ \rho uv\\ \rho v^2+p\\ (\rho e_t+p)v\end{bmatrix}, H=\frac{1}{y}\begin{bmatrix}\rho v\\ \rho uv\\ \rho v^2\\ (\rho e_t+p)v\end{bmatrix}, \tag{3}$$

$$E_v=\begin{bmatrix}0\\ \tau_{xx}\\ \tau_{xy}\\ u\tau_{xx}+v\tau_{xy}-\dot{q_x}\end{bmatrix}, F_v=\begin{bmatrix}0\\ \tau_{xy}\\ \tau_{yy}\\ u\tau_{xy}+v\tau_{yy}-\dot{q_y}\end{bmatrix}, H_v=\begin{bmatrix}0\\ (h_v)_2\\ (h_v)_3\\ (h_v)_4\end{bmatrix}, \tag{4}$$

$$(h_v)_2=\tau_{xy}-\frac{2}{3}\frac{\partial}{\partial x}\left(\mu\frac{v}{y}\right), \tag{5}$$

$$(h_v)_3=\tau_{yy}-\tau_{\theta\theta}-\frac{2}{3}\left(\mu\frac{v}{y}\right)-\frac{2}{3}y\frac{\partial}{\partial y}\left(\mu\frac{v}{y}\right), \tag{6}$$

$$(h_v)_4=u\tau_{xy}+v\tau_{yy}+\frac{\mu}{\Pr(\gamma-1)}\frac{\partial T}{\partial y}-\frac{2}{3}\left(\mu\frac{v^2}{y}\right)-\frac{2}{3}y\frac{\partial}{\partial y}\left(\mu\frac{v^2}{y}\right)-\frac{2}{3}y\frac{\partial}{\partial y}\left(\mu\frac{uv}{y}\right). \tag{7}$$

The stress tensor and heat transfer rate are expressed as follows:

$$\tau_{ij}=\mu\left(\frac{\partial u_i}{\partial x_j}+\frac{\partial u_j}{\partial x_i}\right)+\lambda\left(\frac{\partial u_k}{\partial x_k}\right)\delta_{ij}\,,\ \begin{cases}i=x,y\\ j=x,y\end{cases},\ \lambda=-\frac{2}{3}\mu, \tag{8}$$

$$\tau_{\theta\theta}=\mu\left[-\frac{2}{3}\left(\frac{\partial u}{\partial x}+\frac{\partial v}{\partial y}\right)+\frac{4}{3}\frac{v}{y}\right], \tag{9}$$

$$\mu=\mu_l+\mu_t, \tag{10}$$

$$\dot{q}_i=-\kappa\frac{\partial T}{\partial x_i}, \tag{11}$$

$$\kappa=\kappa_l+\kappa_t. \tag{12}$$

The second viscosity coefficient λ was determined based on Stokes' hypothesis.

2.2 Modeling of Thermal and Chemical Equilibrium

In the case of frozen air, when the air temperature is below 600 K, the following calorically perfect gas equation shown in Eq. (13) becomes the equation of state with a constant specific heat ratio γ, and the viscosity coefficient is typically calculated based on Sutherland's law, as shown in Eqs. (14)–(15) below [6]:

$$p = \rho\left[e_t - \frac{1}{2}(u^2 + v^2)\right](\gamma - 1) = \rho e(\gamma - 1), \tag{13}$$

$$\frac{\mu}{\mu_{ref}} = \left(\frac{T}{T_{ref}}\right)^{\frac{3}{2}} \frac{T_{ref}+S}{T+S}, \mu_{ref} = 1.716 \times 10^5\, kg/m \cdot s, \tag{14}$$

$$T_{ref} = 273.15\, K,\ S = 110.4\, K. \tag{15}$$

When the air temperature reaches 600 K or higher, a vibrational excitation of air molecules occurs; meanwhile, when the temperature reaches 2,000 K or higher, a chemical reaction occurs in the air [7]. In this high-temperature region, the state equation of a calorically perfect gas is no longer valid. In other words, the specific heat ratio γ is no longer constant, and it is a function of the two flow variables, as follows:

$$\tilde{\gamma} = \tilde{\gamma}(\rho, T) = \tilde{\gamma}(\rho, p) = \tilde{\gamma}(p, T). \tag{16}$$

In the present study, the flow temperature was distributed up to 2,500 K, which is essential for considering the vibrational energy and chemical reaction to achieve an accurate calculation. Hence, the air was modeled as a chemically reacting gas, where it was assumed to be in a state of thermal and chemical equilibrium.

To model this air, the thermodynamic properties (e.g., pressure, temperature, and enthalpy) and transport properties (e.g., viscosity and thermal conductivity) should be calculated appropriately. In general, to calculate the equilibrium properties above regardless of the gas type, calculations are to be performed based on statistical thermodynamics. However, in the case of air, it is convenient to use the established data. In this study, the equilibrium properties were calculated using a polynomial-type fitting equation based on previously established data.

First, the thermodynamic properties were calculated using Eqs. (17)–(19). Pressure p is expressed as a function of density and internal energy, whereas temperature T is expressed as a function of pressure and density. Enthalpy h is expressed as a function of pressure and density [8].

$$p = p(e, \rho) = \rho e(\tilde{\gamma} - 1), \tag{17}$$

$$T = T(p, \rho), \tag{18}$$

$$h = h(p, \rho) = \frac{p}{\rho}\left(\frac{\tilde{\gamma}}{\tilde{\gamma}-1}\right). \tag{19}$$

Next, the transport properties can be calculated via a similar procedure using previously established data [9]. The equilibrium transport properties were calculated using the polynomial correlation formulas shown in Eqs. (20)–(22). Each coefficient of the polynomials is tabulated based on the pressure and temperature range, as follows:

$$\mu = A_\mu + B_\mu\chi + C_\mu\chi^2 + D_\mu\chi^3 + E_\mu\chi^4 + F_\mu\chi^5, \tag{20}$$

$$k = \exp[A_K\chi^4 + B_K\chi^3 + C_K\chi^2 + D_K\chi + E_K\ ], \tag{21}$$

$$Pr = A_{Pr} + B_{Pr}\chi + C_{Pr}\chi^2 + D_{Pr}\chi^3 + E_{Pr}\chi^4 + F_{Pr}\chi^5. \tag{22}$$

2.3 Modeling of Turbulence

For turbulence modeling, the standard $k-\varepsilon$ turbulence model [10] was used, and the relevant equations are as follows:

$$\frac{\partial(\rho k)}{\partial t}+\nabla\cdot\left(\rho k\vec{V}\right)=\nabla\cdot\left[\left(\mu_l+\frac{\mu_t}{\sigma_k}\right)\nabla k\right]-\rho\varepsilon+2\mu_t\bar{\bar{E}}\cdot\bar{\bar{E}}, \tag{23}$$

$$\frac{\partial(\rho\varepsilon)}{\partial t}+\nabla\cdot\left(\rho\varepsilon\vec{V}\right)=\nabla\cdot\left[\left(\mu_l+\frac{\mu_t}{\sigma_\varepsilon}\right)\nabla\varepsilon\right]+C_1\frac{\varepsilon}{k}2\mu_t\bar{\bar{E}}\cdot\bar{\bar{E}}-C_2\rho\frac{\varepsilon^2}{k}, \tag{24}$$

$$\mu_t=C_\mu\frac{\rho k^2}{\varepsilon}, \tag{25}$$

where the typical values for the turbulent constants were used, i.e., $\sigma_k=1.00$, $\sigma_\varepsilon=1.30$, $C_1=1.44$, $C_2=1.92$, and $C_\mu=0.09$. This model is suitable for a wall-bounded flow with a low Reynolds number, as in a plasma wind tunnel [2].

2.4 Numerical Scheme

The governing equations were discretized using a finite volume method. The convective flux and diffusion terms were discretized using the AUSMPW+ scheme [11] and a central difference scheme, respectively. A total variation diminishing (TVD) scheme with a minmod limiter was used to achieve high-order spatial accuracy [12]. Furthermore, pseudo-time integration was performed to achieve convergence using the lower-upper symmetric Gauss–Seidel scheme [13]. The iterations were performed until the mass flow imbalance between the inlet and exit of the diffuser was less than 1%.

2.5 Computational Domain and Boundary Conditions

In this study, a flow analysis of the nozzle, test section, and diffuser of the plasma wind tunnel was conducted. The length from the nozzle inlet to the exit of the diffuser was approximately 20 m, and the maximum diameter of the diffuser cross-section was 2 m. Fig. 2 illustrates the calculation domain and applied boundary conditions. The domain of the test section was set to include the outermost streamline of the ejected flow from the nozzle, wherein the flow was not affected by the test section domain despite the under-expanded condition.

The inflow conditions were determined based on the reservoir conditions of the 13 MW arc-heated scramjet test facility (AHSTF) at the NASA Langley Research Center [14]. It was assumed that the total pressure and total temperature of the reservoir were the same as those of the nozzle inlet; meanwhile, the total pressure, total temperature, and mass flow rate were assigned as inflow conditions, as listed in Table 2.

Considering the cooling system of the plasma wind tunnel, a temperature wall boundary condition of 300 K was applied to the test section and diffuser wall. The back-pressure condition was applied to the diffuser exit on the far right of the domain. By controlling it, the pressure ratio of the wind tunnel was controlled.

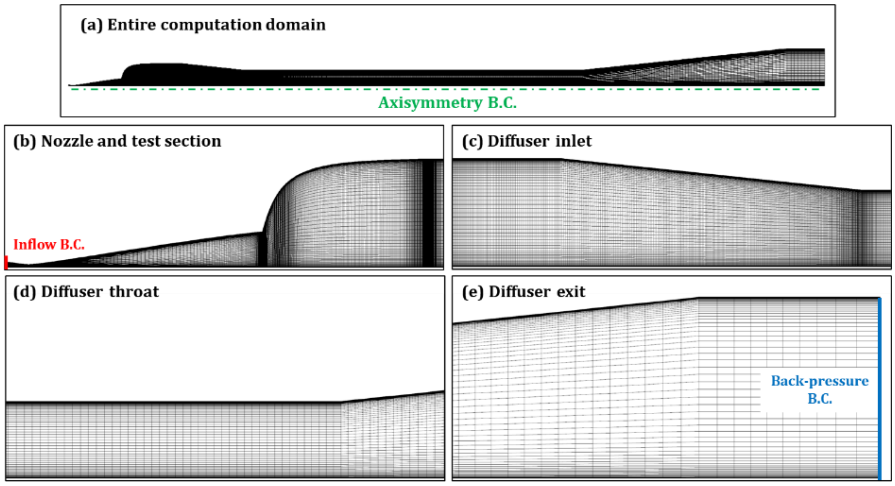

Fig. 2. Configuration of computation domain and boundary conditions applied

Table 1. Flow properties at nozzle inlet and exit

Nozzle inlet (Inflow B.C.)	P_0	28.6 bar
	T_0	2216 K
	$\dot{m}$	2.04 kg/s
Nozzle exit	M	7.0

2.6 Grid Convergence Study

Several grid levels were considered to determine the appropriate grid level. Through preliminary analysis, regions with large gradients of flow variables were identified, and the grid was densely distributed in these regions. The resulting grid was a coarse grid. Subsequently, a uniform refinement of the grid twice in each direction was repeated to obtain medium, fine, and very fine grids. The node dimensions of each grid are presented in Table 3.

By performing a flow analysis based on each grid, the shock wave structure, Mach number, and pressure were confirmed. As shown in Fig. 3, the shock wave structure was damped when a coarse grid was used; however, the difference in the shock wave structure was not significant when a fine grid or higher was used. Fig. 4 shows the axial Mach number and pressure based on the grid level. When the coarse grid was used, the distribution differed significantly; however, when a fine grid or higher was used, no significant difference was observed. Therefore, in this study, the fine grid level was selected considering the grid independence and computational efficiency. At this level, the y+ of the first mesh based on the diffuser throat diameter was distributed at less than 1.

Table 2. Node dimensions of each grid level

Grid level	Node dimension
Coarse	378×23
Medium	756×46
Fine (selected)	1511×91
Very fine	3021×181

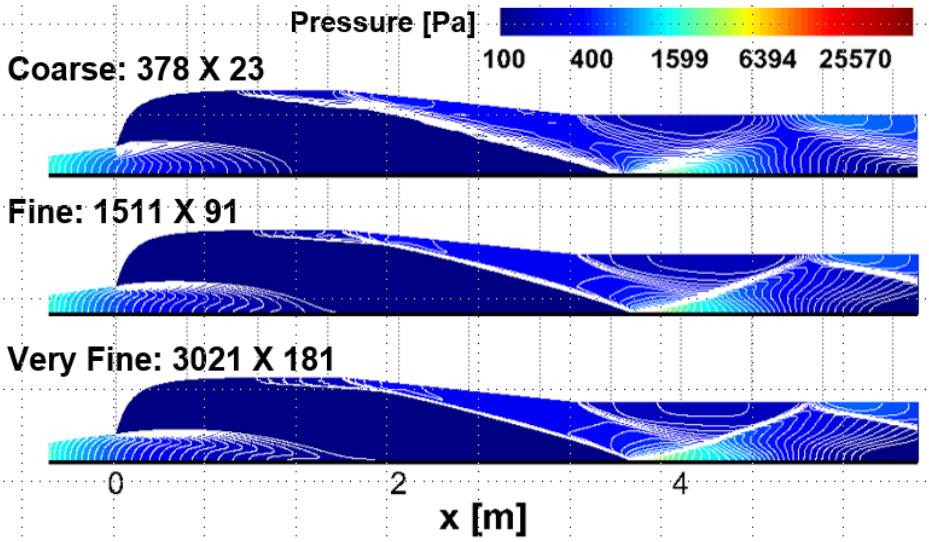

Fig. 3. Shock wave configurations at front section of domain with various grid levels

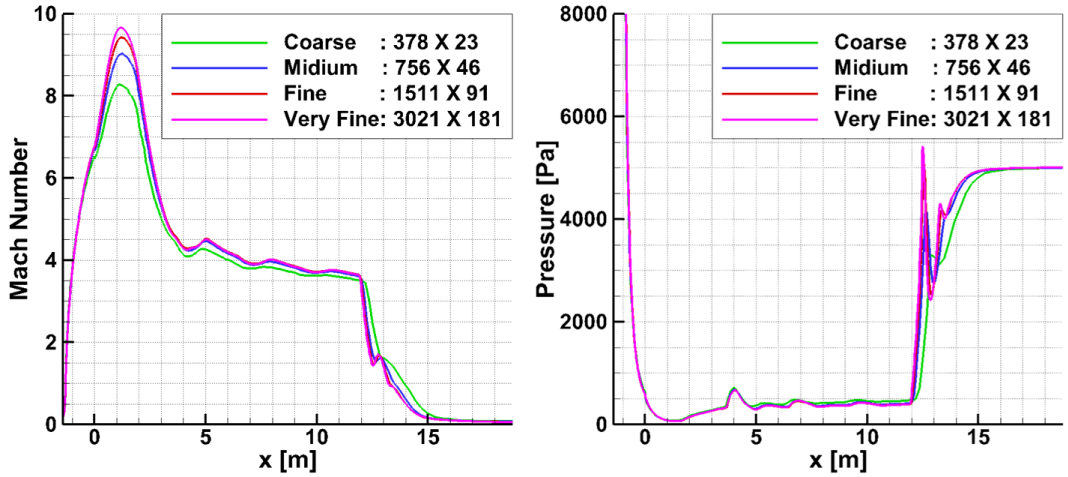

Fig. 4. Mach number (left) and pressure (right) distributions for various grid levels

3 Results and Discussion

3.1 Flow Analysis of Nozzle-Diffuser System

Prior to the analysis of the starting characteristics, the internal flow of the plasma wind tunnel was analyzed under normal operating conditions. Fig. 5 shows the flow characteristics in the nozzle, test section, and diffuser at starting state with a back-pressure of 5,000 Pa. The contour at the bottom of the figure shows the distributions of the static pressure and Mach number. The flow expanded through the nozzle, and a Mach number of 10 or higher was distributed in the test section. Subsequently, a series of oblique shock waves (shock-train) was generated in the diffuser; finally, the flow became subsonic as it passed through a strong terminal shock wave.

The red, blue, and black lines in Fig. 5 represent the trends of the static pressure, Mach number, and total pressure, respectively. As shown by the contour, the flow expanded through the nozzle and test section, and then compressed through the diffuser. It is noteworthy that the initially high value of the total pressure diminished rapidly as the flow passed through the plasma wind tunnel. In particular, a significant total pressure loss occurred owing to the first oblique shock wave formed at the inlet of the

diffuser, and a rapid loss in the total pressure occurred in the terminal shock wave generated at the end of the shock train. Subsequently, the back-pressure and total pressure almost matched at the diffuser exit. The total pressure was diminished in the nozzle and test sections owing to the boundary and shear layers. Meanwhile, the degree of total pressure loss was marginal in the subsonic region in the latter section of the diffuser.

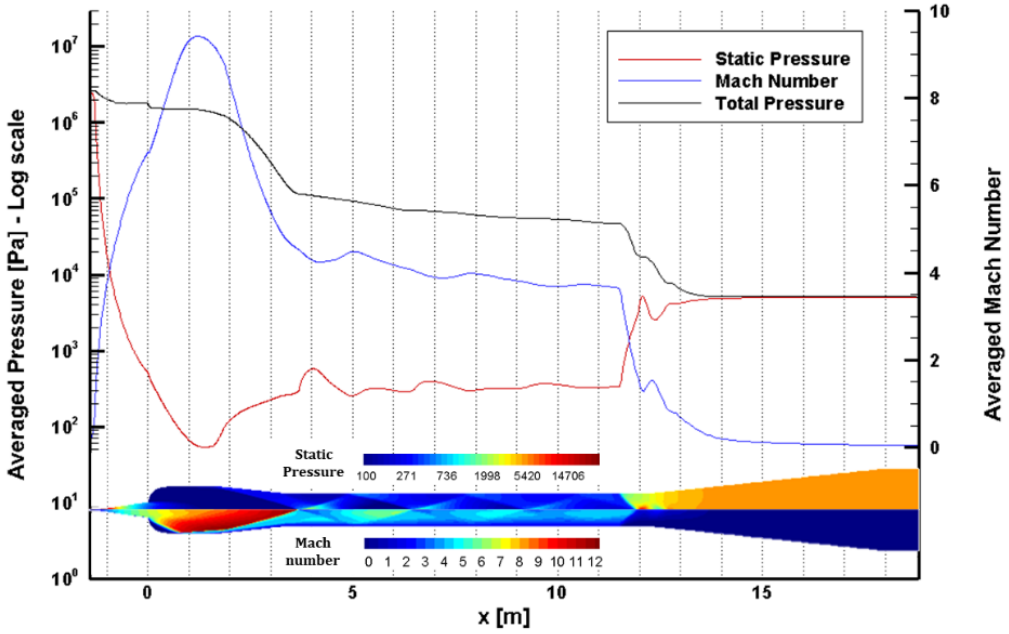

Fig. 5. Flow distributions and trends of pressure, Mach number, and total pressure

3.2 Starting Characteristics

As the pressure ratio of the wind tunnel increased, in other words, as the back-pressure decreased in a fixed reservoir condition, flow occurred inside the wind tunnel. As the pressure ratio increased further, a shock wave was generated at the nozzle throat and a choke formed at the nozzle throat. To start the wind tunnel, a higher pressure ratio must push this initial shock wave past the test section and up to the diffuser throat. This is because the cross-sectional area of the duct increases as the flow propagates toward the test section, and the shock waves at higher Mach numbers generate higher losses. The pressure ratio must be proportional to this loss.

To analyze the starting characteristics, a flow analysis was performed while changing the back-pressure step by step. Because the characteristic time of the back-pressure change is several orders of magnitude larger than the characteristic flow time, the time-dependent starting procedures can be investigated based on a number of steady calculations [1]. First, the calculation converged at a high back-pressure and then converged in stages as the back-pressure reduced until the wind tunnel started. Hence, the starting back-pressure can be determined. After the wind tunnel started, the back-pressure was increased gradually to obtain the maximum operable back-pressure.

Fig. 6 shows the pressure distribution inside the plasma wind tunnel for various back-pressures. Figs. 6 (a)–(d) show the results of sequential convergence while the back-pressure was decreasing; it was observed that the wind tunnel started when the back pressure was 4,000 Pa. Subsequently, the results of sequential convergence while the back-pressure was increasing after the wind tunnel was started are presented in (e) and (f).

When the back pressure was 10,000 Pa, a shock wave was formed inside the nozzle, and as the back pressure decreased gradually, the initial shock wave was pushed downstream. When the back-pressure was 5,000 Pa, a shock wave was formed in the test section, and the flow at the nozzle exit was not sufficiently under-expanded. Subsequently, when the back pressure reached 4,000 Pa, the shock wave was swallowed into the diffuser; at this time, the nozzle exit flow was completely under-expanded, and the test section pressure was maintained at a low level (wind tunnel starting).

Once the shock wave was swallowed into the diffuser and the wind tunnel started, the wind tunnel began to be maintained even after the back-pressure was increased. As shown in Fig. 6. (f), the terminal shock wave was located in the diffuser even when the back-pressure was increased to 5,600 Pa. As such, a history-dependent phenomenon appeared before and after wind tunnel starting, which is known as "hysteresis." In particular, as shown in Figs. 6 (c) and (e), different results were obtained at the same back-pressure.

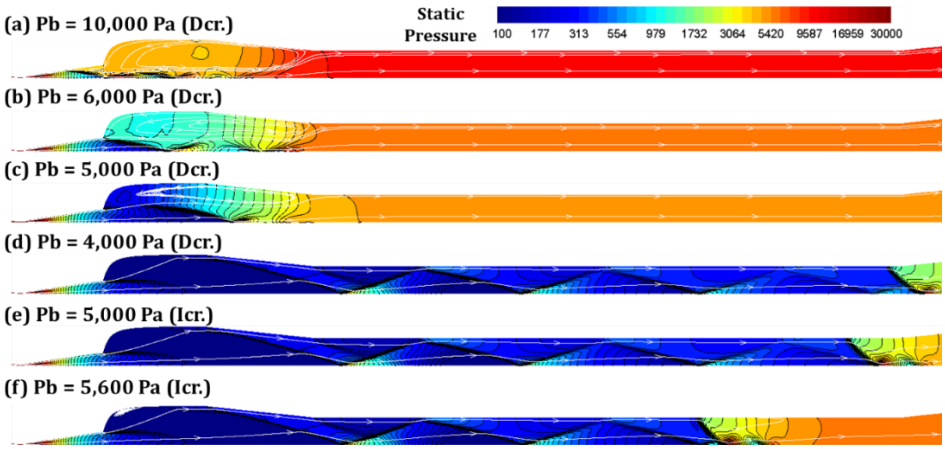

Fig. 6. Pressure distribution at different back-pressures

Fig. 7 shows the test-section pressure history with respect to the back-pressure. The result obtained while decreasing the back pressure is represented by a red line with symbols, and the result obtained by increasing the back pressure is represented by a green line with symbols. Each state in Fig. 6 is marked with a label. As shown in Fig. 7, when the back-pressure was reduced before starting, the wind tunnel started when the back-pressure was at least 4,200 Pa. After starting, it was confirmed that the starting of the wind tunnel remained even when the back-pressure was increased to 5,600 Pa.

As such, hysteresis occurred before and after the start of the plasma wind tunnel. It was assumed that this occurred because when the initial shock wave was swallowed into the diffuser, a series of shock waves was generated, resulting in a lower total pressure loss. As the total pressure loss reduced, the wind tunnel was able to maintain the starting state even when the back pressure was increased. By contrast, before the wind tunnel started, a strong shock wave was generated in the test section, resulting in a relatively significant total pressure loss and a lower back-pressure to start the wind tunnel.

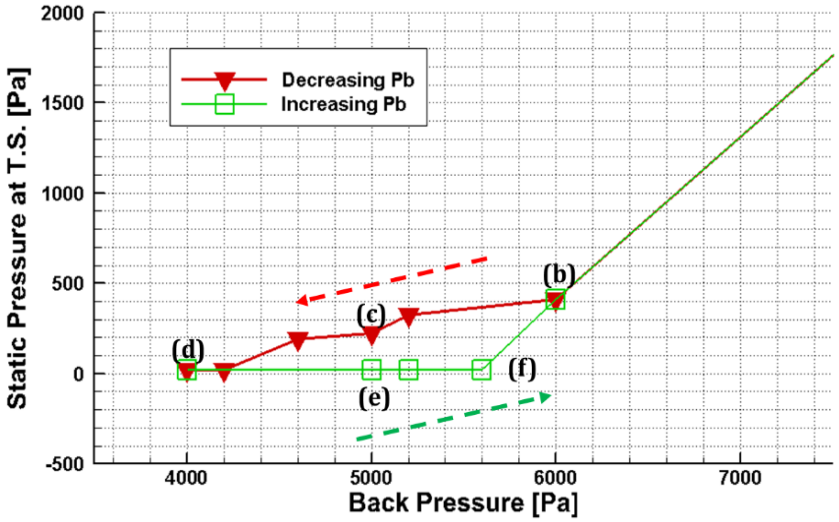

Fig. 7. Static pressure at test section (x = 0.5 m) based on different back-pressures applied

4 Conclusion

In this study, the internal flow and starting characteristics of a nozzle-diffuser system for a plasma wind tunnel were investigated using a computational method. The flow conditions at the reservoir were a total pressure of 28.6 bar and a temperature of 2,216 K, which generated a mass flow rate of approximately 2 kg/s with a Mach 7 nozzle, consistent with the conditions of a megawatt-class large plasma wind tunnel. RANS equations were solved using a two-equation turbulence model and the modeling of equilibrium-state air considering the flow feature.

We conducted a numerical investigation by varying the back-pressure condition or pressure ratio. It was confirmed that the high total pressure of air at the reservoir diminished rapidly as the air passed through the nozzle and diffuser. In particular, severe losses in the total pressure were confirmed in the initial shock wave and the terminal shock wave. Furthermore, it was confirmed that hysteresis occurred before and after the start of the wind tunnel. In other words, a lower back-pressure (i.e., a higher pressure ratio) was required to start the wind tunnel when increasing the pressure ratio before starting the wind tunnel, after which the wind tunnel operation was possible even at a higher back-pressure.

These characteristics should be considered in the design and performance evaluation of a plasma wind tunnel. In future studies, the wind tunnel starting phenomenon should be investigated more comprehensively via an unsteady analysis that reflects the initial driving scenario of the wind tunnel.

Acknowledgements

The Institute of Engineering Research at the Seoul National University provided the research facilities for this study. This study was supported by the National Research Foundation of Korea (NRF) funded by the Ministry of Science and ICT (grant number NRF-2017R1A5A1015311).

References

1. Savino, R., Monti, R. and Esposito, A. (1999) 'Behaviour of hypersonic wind tunnels diffusers at low Reynolds nwaabers', *Aerospace Science and Technology*, (1), pp. 11–19.
2. R.S Pugazenthi and Andy C. McIntosh (2011) 'Design and Performance Analysis of a Supersonic Diffuser for Plasma Wind Tunnel'. doi: doi.org/10.5281/zenodo.1330939.
3. Monti, R. *et al.* (2001) 'Low-Reynolds number supersonic diffuser for a plasma-heated wind tunnel', *Int. J. Therm. Sci*, 40, pp. 804–815.
4. Agostinelli, P. W. *et al.* (2020) 'Investigation of hypersonic flow in the vki h3 wind tunnel: From facility characterization to boundary-layer interaction over low-temperature ablators', in *23rd AIAA International Space Planes and Hypersonic Systems and Technologies Conference, 2020*. American Institute of Aeronautics and Astronautics Inc, AIAA. doi: 10.2514/6.2020-2445.
5. Agostinelli, P. W., Trifoni, E. and Savino, R. (2019) 'Aerothermodynamic analyses and redesign of GHIBLI Plasma Wind Tunnel hypersonic diffuser', *Aerospace Science and Technology*, 87, pp. 218–229. doi: 10.1016/j.ast.2019.02.023.
6. Sutherland, W. (1893) 'The viscosity of gases and molecular force ', *The London, Edinburgh, and Dublin Philosophical Magazine and Journal of Science*, 36(223), pp. 507–531. doi: 10.1080/14786449308620508.
7. Anderson, J. D. (2006) *Hypersonic and High Temperature Gas Dynamics (AIAA Education)*. American Institute of Aeronautics and Astronautics Inc, AIAA.
8. Srinivasan, S., Tannehill, J. C. and Weilmuenster, K. J. (1181) NASA Reference Simplified Curve Fits for the Thermodynamic Properties of Equilibrium Air.
9. Gupta, R. N. et al. (1991) Calculations and Curve Fits of Thermodynamic and Transport Properties for Equilibrium Air to 30000K, NASA Reference Publication 1260.
10. Jones, W. P. and Launder, B. E. (1972) 'The prediction of laminarization with a two-equation model of turbulence', *International Journal of Heat and Mass Transfer*, 15(2), pp. 301–314. doi: 10.1016/0017-9310(72)90076-2.
11. Kim, K. H., Kim, C. and Rho, O. H. (2001) 'Methods for the accurate computations of hypersonic flows. I. AUSMPW+ scheme', *Journal of Computational Physics*, 174(1), pp. 38–80. doi: 10.1006/jcph.2001.6873.
12. Sweby, P. K. (1984) 'High Resolution Schemes Using Flux Limiters for Hyperbolic Conservation Laws', *SIAM Journal on Numerical Analysis*, 21(5), pp. 995–1011. doi: 10.1137/0721062.
13. Yoon, S. and Jameson, A. (1988) 'Lower-upper symmetric-gauss-seidel method for the euler and navier-stokes equations', *AIAA Journal*, 26(9), pp. 1025–1026. doi: 10.2514/3.10007.
14. Witte, D. W. *et al.* (2004) *998 Calibration of the Mach 4.7 and Mach 6 Arc-Heated Scramjet Test Facility Nozzles*. Hampton, Virginia. Available at: http://www.sti.nasa.gov.